Optimizing an acoustic liner by automatic differentiation of a compressible flow solver

Jose I. Cardesa, Romain Fiévet, Estelle Piot, Hugues Deniau, Christophe Airiau

Optimizing an acoustic liner by automatic differentiation of a compressible flow solver

J. I. Cardesa[a,b,*], R. Fiévet[b,c], E. Piot[b], H. Deniau[b], C. Airiau[a]

[a] *IMFT, Université de Toulouse, UMR 5502 CNRS/INPT-UPS, France*
[b] *ONERA / DMPE, Université de Toulouse, F-31055 Toulouse - France*
[c] *Niels Bohr Institute, Blegdamsvej 17, Copenhagen, 2100, Danemark.*

Abstract

The attenuation power of an acoustic liner is optimized by unsteady compressible flow simulations that model the presence of the liner with a time-domain impedance boundary condition (TDIBC). Two test cases are considered: a one-dimensional impedance tube and a two-dimensional grazing incidence tube. The impact of the liner on the pressure field is tuned through various TDIBC parameters imposed at the boundary where the liner surface is located. Automatic differentiation of the direct numerical simulation (DNS) code yields the gradients of the time-integrated pressure perturbations with respect to the TDIBC parameters. The gradients are subsequently used in an iterative process that minimizes the perturbations at a given location. In both test cases considered, TDIBC parameters are found which are more effective at attenuating perturbation frequencies other than those the initial TDIBC is designed to cancel. Finally, a sensitivity analysis reveals the importance of the choice of the initial TDIBC parameters for finding optimized settings. Our results pave the way to a wider application of the presented procedure in more complex problems with bulk flow motion and larger perturbation amplitudes.

Keywords: gradient-based multi-parameter optimisation, automatic differentiation, time-domain impedance boundary condition, acoustic liner.

1. Introduction

Optimizing liners in order to improve their attenuation capacity is the subject of much experimental and theoretical work. One strategy that receives significant attention is that of segmented liners. In early numerical studies, Baumeister[1] analyzed a number of axially segmented liner configurations for liners in a rectangular duct without any mean flow, and concluded that their use fails to offer sufficient advantage over a uniform liner except in low-frequency, single-mode applications. More recently, Law *et al.*[2] reach similar conclusions. By choosing more elaborate liner arrangement combinations which scatter sound towards different modes that are then attenuated by a subsequent

*Corresponding author
Email address: jcardesa@onera.fr (J. I. Cardesa)

stage of liners, Gerhold *et al.*[3] report acoustic performance improvements. Following a rather theoretical approach, Campos *et al.*[4] consider wave convection within a uniform axial flow, where a circumferentially non-uniform but axially uniform wall impedance distribution allows them to speed up axial decay of the slowest decaying wave modes by tuning the circumferential impedance distribution. A different approach found in studies by Nark *et al.*[5, 6] consists of setting a cost function based on in-duct attenuation, and finding its maximum value on a tiled reactance-resistance grid. The process is repeated at several frequencies, and a close-in step on the attenuation maximum is carried out using a finer reactance-resistance grid. The numerous noise propagation calculations induced by this space-sampling approach can be alleviated when using an optimization package external to the flow solver, as done in the more recent studies[7, 8]. It is worth noting that these studies rely on the Ffowcs-Williams and Hawkings analogy for the sound propagation computations. Özkaya *et al.*[9, 10, 11] opt for a rather different computational approach, which deserves mention since it is a direct precursor to our study. They solve the steady flow equations using a commercial computational fluid dynamics (CFD) software, and the obtained mean velocity and pressure fields are given as external input to the computational aeroacoustics (CAA) solver based on the time-dependent linear Euler equations (LEE). The acoustic liner within the CAA framework is modelled according to a 5-parameter extended Helmholtz resonator (EHR), and derivatives of a cost function based on acoustic wave propagation over a time interval are obtained by automatic differentiation (AD) of the CAA solver. Finally, following a gradient descent algorithm, an optimal set of liner parameters can be found. Such an approach has the distinct advantage of allowing for an adjoint-based AD optimization in space that yieds the high-dimensional design gradient vector in one stroke.

The study presented here contrasts with the work on liner optimization previously mentioned in that a fully non-linear and unsteady Euler/Navier-Stokes solver is used without decoupling the flow from the noise computations. Our approach is based on the solution of the governing equations without resorting to acoustic analogies or the linearized Euler equations. Hence, AD is used directly on the DNS flow solver. What is similar to the work of Özkaya *et al.*[9, 10, 11] is that derivatives of a cost function with respect to the acoustic liner parameters are computed, with the cost function to be minimized being defined over a time interval. Unlike Özkaya *et al.*[9, 10, 11], the flow solver is unsteady, relies on a high-order spatial discretization, and the liner is not modelled on the basis of the EHR model. Instead, the oscillo-diffusive representation[12] of the reflection operator at the liner surface is used to model the liner through a time-domain impedance boundary condition[13] (TDIBC). As a counterpoint, it must be stated that – at this stage – the problems considered are simpler in terms of geometric complexity than those treated by Özkaya *et al.*[9, 10, 11], and limited to a design gradient vector of much lower dimensionality – no spatial variability of the liner properties is considered here.

It is important to note that the cases analyzed in this study are chosen so as to place the tools that have been developed in a validation and proof-of-concept environment. The problems that are solved involve small pressure perturbations in the absence of bulk flow, and hence LEE should suffice to obtain the acoustic field. But the methods employed – gradient-descent optimization through AD of a non-linear viscous solver – are indifferent to the physical problem considered. It follows that acoustic propagation cases where the LEE assumptions break down are still within reach of our approach. Such flow problems

are left for future work, and the present study intends to describe the computational procedure and assess its performance in controlled scenarios where it is expected that improved liner properties can be obtained.

The computational tools will be described first in Section 2, followed by the test cases in Section 3. Results will be outlined in Section 4 and discussed in Section 5, before conclusions are brought forward in Section 6.

2. Computational Tools

2.1. Numerical flow solver

The flow solver used in the present study is called JAGUAR[14, 15], which is jointly owned and developed by CERFACS[1] and ONERA. This CFD code uses a spectral difference scheme[16, 17, 18, 19, 20] for the spatial discretization, which belongs to the family of finite element methods. It solves the strong form of the governing equations for a compressible flow. The method allows for an arbitrarily high order of accuracy even on unstructured meshes, and is suited to both compressible or incompressible flow computations. In practice, the scheme reconstructs a polynomial solution of the conservative variables $\mathbf{U} = (\rho, \rho u, \rho v, \rho e)^\intercal$ inside each element with density ρ, streamwise (herein x-coordinate) velocity u, wall-normal (herein y-coordinate) velocity v and specific internal energy e. The polynomial order $\mathtt{p}$ determines the overall scheme's accuracy and computational effectiveness. Throughout this study, $\mathtt{p} = 4$, which results in a fifth-order accurate spectral difference scheme. Furthermore, the time integration follows an optimized low-dissipation low-dispersion fourth order 6-step Runge-Kutta scheme inspired from Berland *et al.*[21]. Finally, all results presented in the following sections are carried out in inviscid (Euler flow) mode in one or two dimensions, so that the governing equations in generalized coordinates (ξ,η) are given by:

$$\frac{1}{\mathcal{J}}\frac{\partial \mathbf{U}}{\partial t} + \frac{\partial}{\partial \xi}\left(\mathbf{E}_c\frac{\xi_x}{\mathcal{J}} + \mathbf{F}_c\frac{\xi_y}{\mathcal{J}}\right) + \frac{\partial}{\partial \eta}\left(\mathbf{E}_c\frac{\eta_x}{\mathcal{J}} + \mathbf{F}_c\frac{\eta_y}{\mathcal{J}}\right) = 0, \tag{1}$$

where $\mathcal{J}$ is the mesh local Jacobian and the convective fluxes of $\mathbf{U}$ in physical space are called ($\mathbf{E}_c$, $\mathbf{F}_c$). We call p the static pressure such that the fluxes read as:

$$\mathbf{E}_c = (\rho u, \rho u^2 + p, \rho v u, (\rho e + p)u)^\intercal \tag{2a}$$

$$\mathbf{F}_c = (\rho v, \rho u v, \rho v^2 + p, (\rho e + p)v)^\intercal \tag{2b}$$

Choosing to set JAGUAR to its inviscid rather than its viscous mode is justified on the basis of the test cases considered which lack bulk flow motion. However, the procedure of automatically differentiating JAGUAR is indifferent to the code being set to viscous or inviscid mode, so that a broader set of flow problems can be considered in the future.

[1] European Center for Research and Advanced Training in Scientific Computation

2.2. Time-domain impedance boundary conditions

In order to capture the effect of the acoustic liner on the flow field, a TDIBC is used as developed in Fiévet *et al.*[13]. It consists of three separate components detailed below as a bulleted list[2]:

- An impedance law $\tilde{z}(s)$, which characterizes the acoustic properties of the coating in Laplace-space ($s = \mathrm{j}\omega$, where j is the complex unit number and ω the angular frequency). For practical reasons, we work with the reflection coefficient $\tilde{B}$ defined in Laplace space as:

$$\tilde{B}(s) = \frac{\tilde{z} - \rho c}{z + \rho c} \tag{3}$$

  where c is the speed of sound. Importantly, the modulus of $\tilde{B}$ is always inferior or equal to unity, which offers interesting stability properties to a $\tilde{B}$-based TDIBC as opposed to a $\tilde{z}$-based one, as shown by Monteghetti *et al.*[22].

- A discretized representation of $\tilde{B}$, referred to as $\tilde{\beta}$. This representation consists in a delayed multi-pole approximation[12] which models a single-degree of freedom acoustic liner – the kind used throughout the present study. It relies on N_s oscillatory and N_ν diffusive poles, and is defined as follows:

$$\widetilde{\beta}(s) = \beta_\infty + \sum_{n=1}^{N_s} \frac{\widetilde{r}_{1,n}}{s - \widetilde{s}_n} + \sum_{k=1}^{N_\nu} \frac{\mu_{1,k}}{s + \nu_k} + e^{-s\tau} \left(\sum_{n=1}^{N_s} \frac{\widetilde{r}_{2,n}}{s - \widetilde{s}_n} + \sum_{k=1}^{N_\nu} \frac{\mu_{2,k}}{s + \nu_k} \right). \tag{4}$$

  $\tilde{\beta}$ depends on a parameter vector q that includes the bulk reflectivity β_∞, a time delay τ related to the depth of the liner cavities, the oscillatory weights $\widetilde{r}_{1,n}$ and $\widetilde{r}_{2,n}$, the oscillatory poles $\widetilde{s}_n$, the diffusive weights $\mu_{1,k}$ and $\mu_{2,k}$, and the diffusive poles ν_k. The more poles are used, the more broadband-accurate the representation can become.

- A semi-discrete formulation of this impedance condition in the time-domain to couple itself with the internal flow solver. In JAGUAR, the TDIBC is implemented in characteristic form using a time-domain scattering operator $\mathcal{B}$. This amounts to evaluating the amplitude of the incoming characteristic at the boundary as a function of the outgoing characteristic according to:

$$\partial_t p + (\rho c)\partial_t \mathbf{u}.\mathbf{n} = \mathcal{B}[\partial_t p - (\rho c)\partial_t \mathbf{u}.\mathbf{n}] = \hat{\tilde{\beta}} \star [\partial_t p - (\rho c)\partial_t \mathbf{u}.\mathbf{n}], \tag{5}$$

  where $\mathbf{u}.\mathbf{n}$ is the velocity normal to the boundary and $\hat{\tilde{\beta}}$ is the inverse Laplace transform of $\tilde{\beta}$. The operator $\mathcal{B}$ is evaluated by transforming the convolution product into a sum of $(N_s + N_\nu)$ auxiliary variables, *i.e.* one per acoustic pole, each solution of an ordinary differential equation[22] defined by the parameters inside vector q.

[2]For clarity, all complex numbers are written with a tilde, while exclusively real-valued ones are not.

A thorough presentation of the TDIBC development is given in Monteghetti *et al.*[22]. For a validation and verification of the numerical implementation of the TDIBC, the reader is referred to Fiévet *et al.*[13], which includes a detailed explanation of its deployment within a spectral difference flow solver such as JAGUAR. With regards to the present study, the important point is that the TDIBC is an explicit function of a finite set of both real and complex parameters contained inside q.

2.3. Automatic differentiation

Gradient-based methods play an important role in the process of seeking those conditions that modify the solution of a physical problem towards a specific goal, either for optimization or control purposes. Computing the necessary gradients (also referred to as sensitivities) is a task that can be automated by automatic differentiation (AD) tools. In short, AD augments a given "primal" code that initially computes outputs Y_i from inputs X_j into a "differentiated" code that additionally computes some derivatives dY_i/dX_j requested by the user. AD provides two main modes, the tangent/direct/forward mode and the adjoint/reverse/backward mode. If i and j are the indices along the output and input spaces, respectively, bound so that $1 \leq i \leq m$ and $1 \leq j \leq n$, then the tangent mode is most efficient when $n \ll m$ while the adjoint mode is the only realistic option for $m \ll n$.

Over the years, the AD community has produced a number of tools to generate differentiated code based on different strategies, chiefly operator overloading (OO) and source transformation (ST). Perhaps the most important point to bear in mind when choosing an AD tool is the programming language in which the primal code is written. JAGUAR is written following features from the Fortran 90 standard onward, which narrows down our choice of an AD tool towards an effective and well established ST-based open-source software: TAPENADE[23]. In a previous study[24], the compatibility between TAPENADE and JAGUAR was verified and the performance of the differentiated code in both tangent and adjoint modes was assessed for gradient computations. In particular, it was shown that the computational cost of the adjoint-differentiated code was above 15 times that of the primal code, while for the tangent-differentiated code the same factor was reduced to 1.7. Both numbers refer to the cost of running JAGUAR in explicit time-integration mode to compute one sensitivity. The conclusion from those numbers is that the adjoint-mode differentiation begins to pay off when more than 15 sensitivities are required in a single code execution. Since the flow problems that are solved further down involve computing gradients in 14-dimensional space at most, the (vector) tangent mode is chosen. For ease of implementation, the serial version of JAGUAR is chosen for differentiation over the parallel version.

3. Problem Setup

In the present section, the two considered test cases are described and the common optimization procedure is explained. Both test cases are computed assuming inviscid flow, time-integrated using a constant time step size, and spatially-discretized with a fifth-order approximation ($\mathtt{p} = 4$).

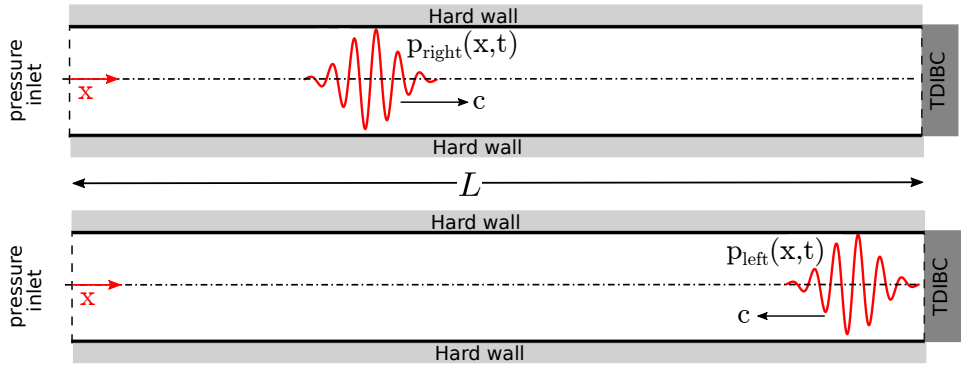

Figure 1: Sketch of the 1D impedance tube test case. The inlet packet of pressure fluctuations travels towards positive x at the sound speed c *(top)*. At $x = L = 1.8$ m, a TDIBC is located which interacts with the incident wave packet, reflecting it back towards the inlet *(bottom)*.

3.1. Wave packet in a 1D impedance tube

A one-dimensional problem representing a tube of length $L = 1.8$ m is considered, open at $x = 0$ and closed with a TDIBC at $x = L$. A sketch is provided in Fig. 1. The pressure in the tube is at its ambient value $p_a = 101325$ Pa. At $t = 0$, a pressure wave packet enters the tube at $x = 0$, travelling at the speed of sound $c = 344.37$ m/s towards $x = L$. The properties of the wave packet are illustrated in Fig. 2 and detailed in its caption. It is emphasized that the input pressure perturbations are broadband throughout the present study. The spatial discretization relies on $N_x = 60$ grid points,

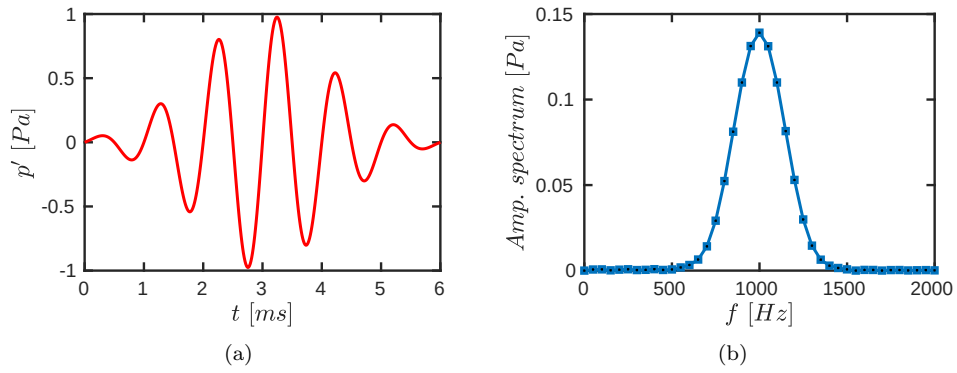

Figure 2: (a) Time series of the pressure perturbation of the incident wave packet signal and (a) its corresponding single-sided amplitude spectrum. The input wave packet for a chosen frequency f is given by $p' = A \sin(2\pi f\,(t - 3/f)) \exp\left(-\sigma^2 f\,(t - 3/f)^2\right)$. For all cases considered in the present study, $A = 1$ Pa, $\sigma^2 = 400$. The two figures above were based on $f = 1000$ Hz, but input wave packets with $f = 1500$ Hz and $f = 2000$ Hz are also employed in this study.

resulting in a constant grid spacing of $\Delta x = 3.051 \times 10^{-2}$ m and a Nyquist frequency of $c/(2\Delta x) = 5643$ Hz. As can be seen in Fig. 2(b), the amplitude spectrum of the input wave packet shows no energy well before reaching the Nyquist frequency.

A probe at $x = 0.3$ m records the pressure fluctuations p' with respect to p_a observed in Fig. 3. The pressure fluctuations induced by the input wave packet are those recorded during the interval between $t = 0$ and $t_1 = 8 \times 10^{-3}$ s. The second wave packet recorded by the probe during $t_1 \leq t \leq t_2$ corresponds to the pressure waves reflected by the TDIBC while they travel back towards $x = 0$. The simulation ends at t_2, reached by setting a constant time step $\Delta t = 7 \times 10^{-7}$ s and running for 25000 time steps. It is worth emphasizing that the ability to resolve accurately pressure perturbations of the order of 1 Pa with respect to ambient pressure, as done in the present study, illustrates the suitability of the high-order code JAGUAR at tackling acoustic propagation problems.

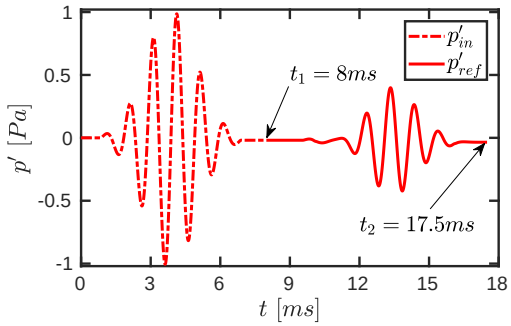

Figure 3: Pressure perturbations p' measured about the ambient value $p_a = 101325$ Pa at the probe location $x = 0.3$ m. The oscillations for $t < t_1$ are due to the incident wave packet characterized in Fig. 2 travelling from the inlet at $x = 0$ towards the TDIBC wall at $x = 1.8$ m. The interval between t_1 and t_2 is chosen to study the properties of the pressure perturbations reflected by the TDIBC back towards the inlet.

3.2. Wave packet grazing over an acoustic liner

The second test case is inspired on the grazing incidence tube (GIT) experiment of Jones *et al.*[25]. In that experiment, a three-dimensional tube with square cross-section is used to collect reference data for validation of acoustic propagation codes.

In the present study, the domain is discretized with a two-dimensional mesh. A sketch of the setup for this test case is provided in Fig. 4. As can be seen in that figure, the presence of an acoustic liner at the bottom wall is modelled with a TDIBC that interacts with the input right-running pressure waves. A regular grid with constant $\Delta y = 4.5$ mm and $\Delta x = 4.2$ mm was chosen, leading to a Nyquist frequency of 37875 Hz. The same grid is used in a previous study[13], where a harmonic plane pressure wave at 2000 Hz is input at the inlet of the domain. In the present study, a Gaussian plane wave packet is used with properties as those displayed in Fig. 2, but with a peak amplitude spectrum centered at 1500 Hz instead of 1000 Hz as that shown in Fig. 2(b). The transient evolution

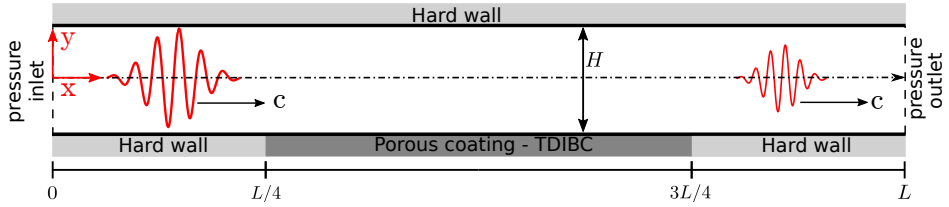

Figure 4: Sketch of the grazing incidence tube (GIT) test case. $L = 812$ mm, $H = 50$ mm. The right running pressure waves are damped under the effect of the TDIBC on the lower wall.

of the pressure fluctuations in the domain can be seen on the sequence in Fig. 12. All computations for this test case are carried out with a constant time step of 2×10^{-6} s for 5005 time steps.

3.3. Optimization process

In both test cases previsouly described, JAGUAR imposes a TDIBC at a boundary by relying on a vector q of values for the coefficients of the ODR of the reflection operator found in Eq. (4). The initial inputs of q, which are displayed in the left-hand column of Table 1 as q_{ref}, have been chosen to match the acoustic properties of the ceramic tubular liner (CT57) found in Jones *et al.*[25] by methods outlined in the work of Monteghetti[22]. When comparing Eq. (4) and Table 1, it can be observed that the sums in Eq. (4) are limited to $N_\nu = 0$ and $N_s = 4$, reducing the number of input parameters controlling the TDIBC to 14 – the dimension of q.

For better compatibility with the automatic differentiation step, JAGUAR has to be mildly modified so that a top-level subroutine explicitly takes the 14 control parameters of vector q as input, computes the flow solution by integrating the Euler equations in time, and then returns a scalar cost function as output. The cost function is defined as follows:

$$J(q) = \int_{t_1}^{t_2} \left[p'(q,t) - p'_{tar}(t)\right]^2 \, dt, \tag{6}$$

where $p'_{tar}(t)$ is the target perturbation pressure signal, while $p'(q,t)$ is the perturbation pressure signal obtained with input q. Both pressure signals are measured at a fixed location. For the 1D impedance tube, $x = 0.3$ m is chosen, while for the 2D GIT case the probe location is on the wall opposite to the TDIBC and between the streamwise position of the TDIBC end and the outlet: $x = 70$ cm and $y = 5$ cm – see Fig. 4. In general, optimizing the pressure fluctuations at a single point may lead to generating locally a pressure node. However, that possibility is ruled out in the flow-less test cases considered due to the fact that the outlet is perfectly non-reflecting, so that no standing waves are created after the plane waves employed as input have passed by.

The limits of the time integral in Eq. (6) are chosen so as to contain the temporal window during which the wave packet goes through the probe location. For the 1D impedance tube, t_1 and t_2 are as displayed in Fig. 3. In the GIT experiment, $t_1 = 1.5$ ms and $t_2 = 10$ ms.

While $p'_{tar}(t)$ can in general be a function of time, we choose it to remain fixed so that $p'_{tar}(t \geq t_1) = p'_{ref}(t = t_1)$. The choice is entirely driven by our goal to reduce

parameter	q_{ref}	q_{opt}	q_{opt2}
β_∞	5.000000000000000e-01	6.834083466134500e-01	5.000000000000000e-01
τ	4.799390000000000e-04	4.799390000000000e-04	4.799390000000000e-04
Re($\tilde{s}_1$)	-3.816516000000000e+03	-3.816516030588480e+03	-4.087437807160580e+03
Im($\tilde{s}_1$)	4.734560000000000e+03	4.734559986268240e+03	4.432722825189820e+03
Re($\tilde{r}_{1,1}$)	-7.194232000000000e+02	-7.194231530395811e+02	-1.356788077181370e+03
Im($\tilde{r}_{1,1}$)	-5.447907000000000e+02	-5.447906901955140e+02	-2.630733085844980e+02
Re($\tilde{r}_{1,2}$)	-7.179701000000000e+03	-7.179700991236490e+03	-7.531526389212660e+03
Im($\tilde{r}_{1,2}$)	-7.336684000000000e+03	-7.336684005827590e+03	-7.152990431244080e+03
Re($\tilde{s}_2$)	-2.765741000000000e+04	-2.765740999408590e+04	-2.751836204100200e+04
Im($\tilde{s}_2$)	2.000290000000000e+04	2.000290001185000e+04	2.010326888065210e+04
Re($\tilde{r}_{2,1}$)	1.625807000000000e+03	1.625806932942120e+03	-2.426548543034030e+02
Im($\tilde{r}_{2,1}$)	9.996580000000000e+01	9.996580359397110e+01	-3.098869458748290e+02
Re($\tilde{r}_{2,2}$)	1.614688000000000e+04	1.614687998865900e+04	1.592326890748080e+04
Im($\tilde{r}_{2,2}$)	1.930627000000000e+04	1.930627000791980e+04	1.949584657918380e+04

Table 1: Input quantities parametrizing the TDIBC properties for the case where $N_\nu = 0$ and $N_s = 4$ in Eq. (4). The missing poles and their corresponding weights are the complex conjugate of already-given poles and weights: $\tilde{s}_3 = \bar{\tilde{s}}_1$, $\tilde{s}_4 = \bar{\tilde{s}}_2$, $\tilde{r}_{1,3} = \bar{\tilde{r}}_{1,1}$, $\tilde{r}_{1,4} = \bar{\tilde{r}}_{1,2}$, $\tilde{r}_{2,3} = \bar{\tilde{r}}_{2,1}$, $\tilde{r}_{2,4} = \bar{\tilde{r}}_{2,2}$. The left-hand column displays the values found in Monteghetti[22] to match the experimentally-measured reactance properties in Jones[25]. The middle column contains the values after optimization in the 1D impedance tube when all elements of q can be changed except for τ, while the right-hand column is obtained by keeping both τ and β_∞ constant.

the pressure perturbations damped by the TDIBC. In the optimization procedure that follows, the goal is to find the set of input parameters q_{opt} that brings $p'(q,t)$ closest to p'_{tar}, in other words q_{opt} should minimize J. Since we aim to minimize the pressure perturbations, the chosen p'_{tar} appears to be an ideal target. Of course one has no guarantee that it is realizable, yet exploring how close one may come to it is of great interest.

Once JAGUAR contains the top-level subroutine where the dependence between the input vector q and the scalar output $J(q)$ has become explicit, the subroutine can be automatically differentiated with TAPENADE using vector tangent mode. The differentiated top-level subroutine not only outputs the scalar $J(q)$, but also a vector dJ which contains the sensitivities of J with respect to each element in q. A validation of the sensitivities obtained with AD is performed for the 1D impedance tube by comparing them against finite-difference (FD) approximations. Both estimates of the same sensitivities are displayed in Table 2 and are found to agree reasonably well. The FD estimates are obtained by successive additional runs of JAGUAR (in its non-differentiated form) while changing one element of q at a time. Each element of q is increased by multiplying it times $(1 + 10^{-5})$. The agreement between FD and AD is sufficient to validate the differentiation procedure, yet perceptible differences are to be expected since FDs suffer from truncation error while AD estimates do not. In terms of CPU time, FD requires 14 additional code executions to compute 14 derivatives. The differentiated version of Jaguar was found to require the equivalent of 11.6 additional code executions to provide all 14 sensitivities – 1 code execution takes approximately 56 s on a desktop computer. So not only is the AD more accurate at computing sensitivities, it is also faster – two distinct advantages when it comes to converging towards a minimum through gradient descent algorithms.

The AD-obtained sensitivities are embedded into the following steepest descent loop:

$$q^{n+1}(m) = q^n(m) - \lambda \left[dJ(m)\right]^n, \tag{7}$$

where m is the index of the element within vectors q and dJ, while n is the iteration number. The parameter λ is a fixed "small" number, chosen based on the rate of convergence for each test case.

The values obtained during updates of q in Eq. (7) need to be checked at every iteration so that they comply with the following conditions:

- the real part of the oscillatory poles $\tilde{s}_{1\to4}$ has to remain negative
- the modulus $|\widetilde{\beta}(s)|$ has to remain below or equal to unity for all explored frequencies. In practice, we checked all frequencies between zero and 5650 Hz.

The upper bound of the frequencies checked is chosen based on the Nyquist frequency being 5643 Hz for the 1D impedance tube, and the fact that the amplitude spectrum of the input pressure perturbations is as shown in Fig. 2(b) – negligible energy is found above 3000 Hz. The same frequency check is used in the 2D GIT case since similar input wave packets were used – with $f = 1500$ Hz instead of 1000 Hz as in Fig. 2(b).

4. Results

The results obtained during the optimization under different conditions are presented next, listing simply the findings. A discussion of the results including their interpretation is delayed until Section 5.

4.1. 1D impedance tube

The first problem to be tested by means of the optimization procedure outlined in subection 3.3 is the 1D impedance tube. The descent algorithm in 14-dimensional space following Eq. (7) converges very quickly towards a trivial solution that relies on increasing τ. Such a tendency towards attenuating the energy of the reflected pressure perturbations at $x = L$ by lengthening the delay in the TDIBC response τ is clear from Table 2, where $dJ/d\tau$ is found to be orders of magnitude larger than the other sensitivities. However, it corresponds to an unphysical solution consisting of an infinite-depth liner. Indeed, the delay τ describes the back-and-forth time of an acoustic wave travelling at the speed of sound inside the porous material. Hence τ must remain small enough to ensure that the coating remains thin enough for practical reasons, and so it is decided to exclude τ from the tunable parameters thereby removing it from the optimization procedure. That is the reason why $q_{ref}(2) = q_{opt}(2)$ in Table 1.

With constant τ but all other elements in q left free to vary, the optimization loop always stops around $J(q)/J(q_{ref}) = 0.5$. Loop termination is triggered by the $|\widetilde{\beta}(s)| \leq 1$ constraint being violated at zero frequency. Fig. 5(a) displays that within 7 iterations, the steepest descent algorithm with $\lambda = 10$ can lead to a reflected wave packet that has half the energy of that in the reference case. Smaller values of λ marginally decrease the final J, and the reflected $p'(q_{opt}, t)$ found with $\lambda = 1$ (leading to $J(q_{opt})/J(q_{ref}) = .473$) is shown in Fig. 5(b) along with p'_{ref} and p'_{tar}. The impedance and reflection properties of the TDIBC based on q_{ref} and q_{opt} are shown in Fig. 6, along with the data from Jones *et al.*[25] that has been digitized from Fig. 11 in Monteghetti[22]. Clearly, the optimization

sensitivity	FD	AD
$dJ/d\beta_\infty$	-8.88437693e-03	-8.80614433e-03
$dJ/d\tau$	-9.99960533e-01	-9.99961225e-01
$dJ/d\,[\mathrm{Re}(\tilde{s}_1)]$	9.96196468e-07	9.87109824e-07
$dJ/d\,[\mathrm{Im}(\tilde{s}_1)]$	2.05150921e-07	2.03161660e-07
$dJ/d\,[\mathrm{Re}(\tilde{s}_2)]$	-2.27573528e-06	-2.25552551e-06
$dJ/d\,[\mathrm{Im}(\tilde{s}_2)]$	1.51055213e-08	1.50151825e-08
$dJ/d\,[\mathrm{Re}(\tilde{r}_{1,1})]$	-4.26433793e-07	-4.22653964e-07
$dJ/d\,[\mathrm{Im}(\tilde{r}_{1,1})]$	2.88853903e-07	2.86285441e-07
$dJ/d\,[\mathrm{Re}(\tilde{r}_{1,2})]$	-2.30235872e-07	-2.28195227e-07
$dJ/d\,[\mathrm{Im}(\tilde{r}_{1,2})]$	-4.60166429e-07	-4.56093751e-07
$dJ/d\,[\mathrm{Re}(\tilde{r}_{2,1})]$	2.31226156e-06	2.29169554e-06
$dJ/d\,[\mathrm{Im}(\tilde{r}_{2,1})]$	-3.56872780e-07	-3.53197415e-07
$dJ/d\,[\mathrm{Re}(\tilde{r}_{2,2})]$	4.03100470e-07	3.99515228e-07
$dJ/d\,[\mathrm{Im}(\tilde{r}_{2,2})]$	-2.82792546e-07	-2.80287251e-07

Table 2: Sensitivities of J computed at $q = q_{ref}$ through finite differences (FD) and automatic differentiation.

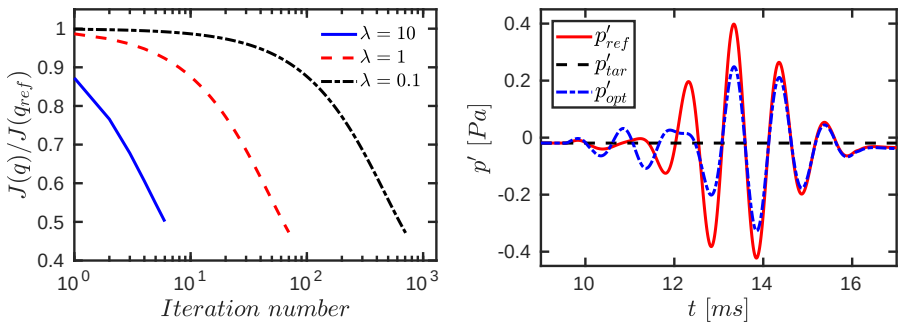

(a) (b)

Figure 5: Optimization at constant τ. (a) Convergence of $J(q)$ towards a minimum value during the gradient descent optimization. For all three values of λ, the optimization algorithm is stopped due to the condition $|\widetilde{\beta}(s)| \leq 1$ being violated at zero frequency after $\{7, 71, 708\}$ iterations for $\lambda = \{10, 1, 0.1\}$, respectively. (b) Reflected pressure perturbations: reference ($q = q_{ref}$), optimized (found with $\lambda = 1$, $q = q_{opt}$ from Table 1) and target p'_{tar}.

process has modified the reactance properties of the TDIBC. Yet looking carefully at the differences between q_{ref} and q_{opt} in Table 1, it appears that the optimization at constant τ has essentially increased β_∞ and left the other elements of q_{ref} unchanged in comparison. Partly because of this, partly because $dJ/d\beta_\infty$ is several orders of magnitude larger than the other sensitivities in Table 2, we explore how the optimization proceeds when we apply the further contraint of keeping β_∞ constant – on top of keeping τ constant.

The result of the optimized q for constant τ and β_∞ is q_{opt2}, and it is displayed in Table 1. Clearly, the elements of q other than β_∞ and τ have now significantly changed. $J(q_{opt2})/J(q_{ref})$ is decreased down to 0.55% as opposed to $J(q_{opt})/J(q_{ref}) = 47.3\%$, proving that major improvements during the optimization can be gained by constraining β_∞ to remain constant. The decrease in J as the steepest descent algorithm proceeds

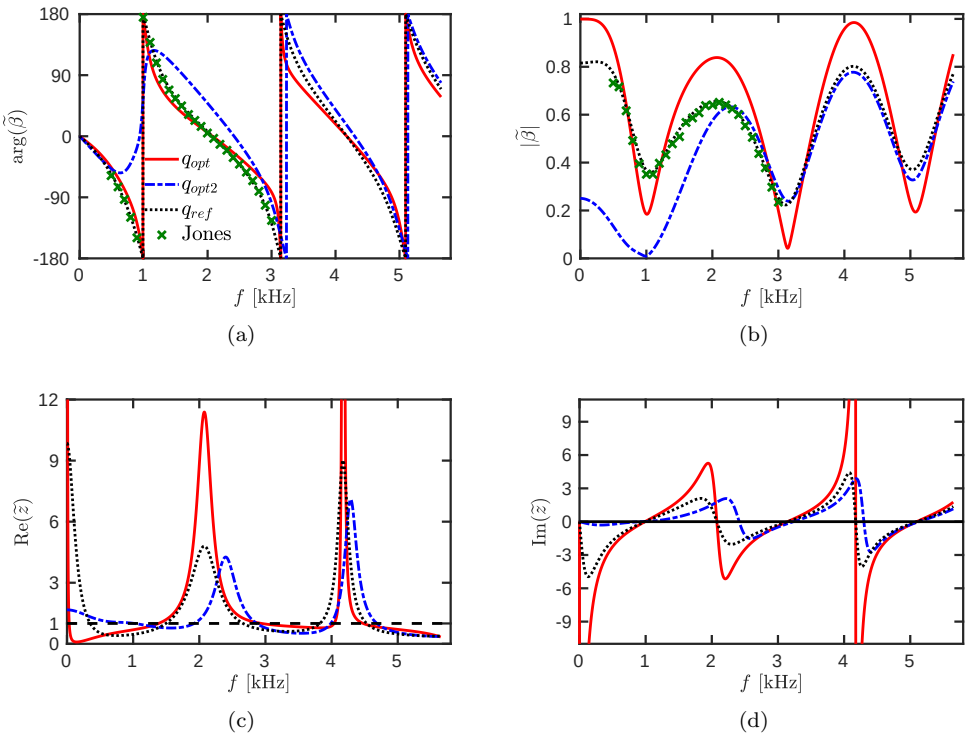

Figure 6: (a) Argument and (b) modulus of the reflection coefficient $\widetilde{\beta}(s)$ based on q_{ref}, q_{opt} and q_{opt2} in Table 1. (c) Real and (d) imaginary part of the impedance $\widetilde{z}(s)$ based on q_{ref}, q_{opt} and q_{opt2}. $\widetilde{z} = (1+\widetilde{\beta})/(1-\widetilde{\beta})$.

can be seen in Fig. 7(a), and the optimized reflected perturbation pressure is shown in Fig. 7(b). The impedance and reflection properties based on q_{opt2} are shown in Fig. 6.

The optimization process used so far is carried out for an input wave packet with an amplitude spectrum centered around 1000 Hz. The optimized parameters in the TDIBC in Table 1 should correspond to an improved tubular ceramic liner that is tuned for the perturbation spectrum considered in Fig. 2. Two other broadband input spectra are considered next for the pressure perturbations, with $f = 1500$ Hz and $f = 2000$ Hz – see the caption of Fig. 2 for the exact dependence of p' on f. The input and the reflected perturbations at the probe location of the 1D impedance tube are shown in Fig. 8 for the three frequencies considered. The optimization procedure is applied to each input frequency, yielding the convergence properties displayed in Fig. 9. It can be observed that the optimization is able to proceed further for the two lower frequencies than for the highest one. The frequency-dependent optimized TDIBC settings, q_{opt3}, are shown in Table 3, and the corresponding impedance and reflection properties are gathered in Fig. 10. Finally, the original and optimized reflected perturbations are displayed in Fig. 11. It should be noted that in the case of the frequency-dependent optimization

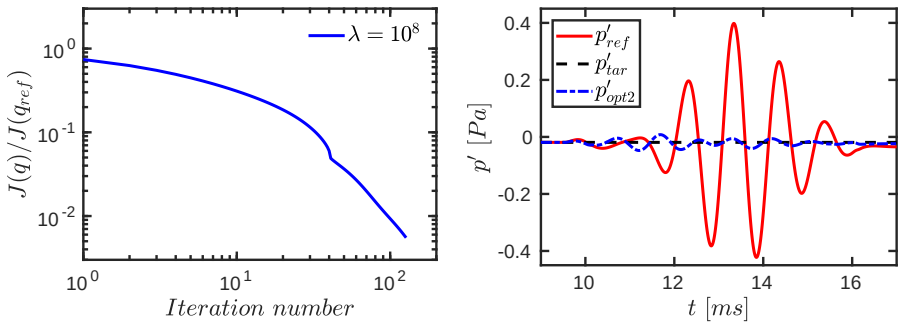

(a) (b)

Figure 7: Optimization at constant τ and β_∞. (a) Convergence of $J(q)$ towards a minimum value during the gradient descent optimization. For $\lambda = 10^8$, $J(q)/J(q_{ref})$ reaches 0.55% before the descent algorithm starts oscillating. We take q_{opt2} to be q recovered after 128 iterations. (b) Reflected pressure perturbations (reference and optimized), and target perturbation level p'_{tar}.

leading to q_{opt3}, the target pressure perturbation p'_{tar} is chosen to be the temporal mean of p'_{ref} between t_1 and t_2, as opposed to a constant value of $p'_{ref}(t_1)$. That is the reason why the q_{opt3} values on the left-hand column of Table 3 do not match those in the right-hand column of Table 1, and why p'_{tar} coincides with p'_{ref} at the beginning in Figs. 5(b) and 7(b), but not in Fig. 11. One can see from Fig. 11 that p'_{tar} is somewhere in between p'_{ref} at the beginning and end of the displayed time window.

It is perhaps the appropriate point to illustrate that a pressure drift takes place, whereby the pressure in the tube decreases after the perturbations have gone past the probe location. The drift is most apparent at the highest input perturbation frequency, as can be seen in Fig. 11. This minor pressure drift is a well-known consequence of using a characteristic boundary condition which only balances out the perturbation field. A typical example is that of a non-reflecting boundary condition ($\mathcal{B} = 0$) which will *perfectly* cancel-out the entering pressure wave but will not enforce any mean pressure value. That is, the computational domain receives no pressure feedback from the outside and the mean pressure field is free to depart from its initial state. This is typically addressed by adding a linear relaxation term as in Poinsot and Lele[26], at the expense of causing mild acoustic reflections as the boundary stiffness increases. Adding a linear relaxation term would modify the boundary's acoustic impedance profile, the accuracy of which is of paramount importance to the present study. Therefore, a minor pressure drift – amounting to one-millionth of the bulk pressure – is deemed acceptable.

4.2. 2D GIT flow

The setup described in subsection 3.2 is considered next. At the probe location ($x = 70$ cm and $y = 5$ cm in Fig. 4), the pressure perturbations are measured and used for the optimization procedure that seeks to bring them closest to a target level p'_{tar}. The initial parameters determining the TDIBC behavior are those in q_{ref} of Table 1. With these initial values, the plane wave packet can be seen in Fig. 12 propagating from

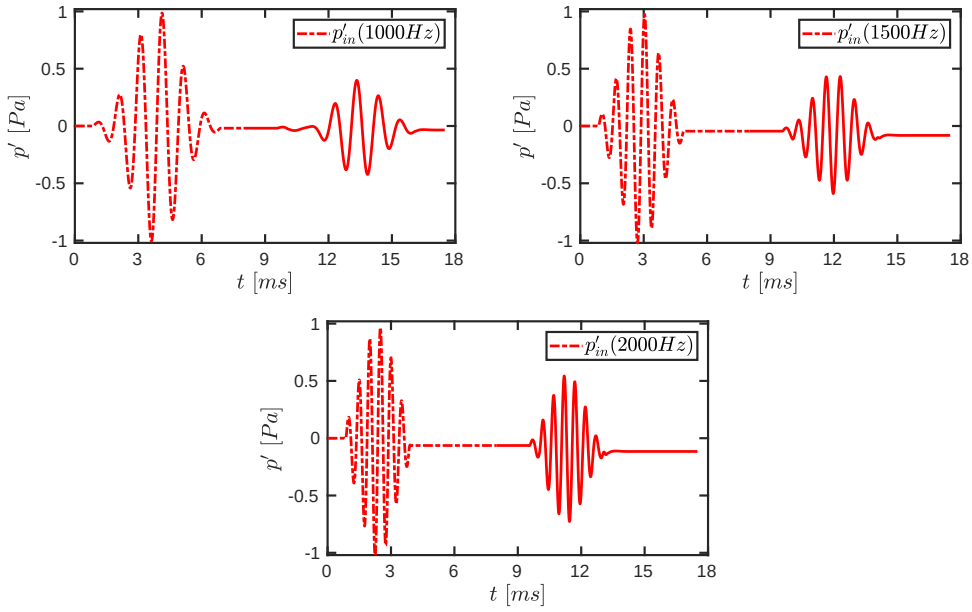

Figure 8: Pressure perturbations p' measured about the ambient value $p_a = 101325$ Pa at the probe location $x = 0.3$ m in the 1D impedance tube. Dashed lines correspond to the right-running wave packet coming from the inlet, while the solid portion corresponds to the perturbations reflected by the TDIBC operating with parameters set at q_{ref} – see Table 1.

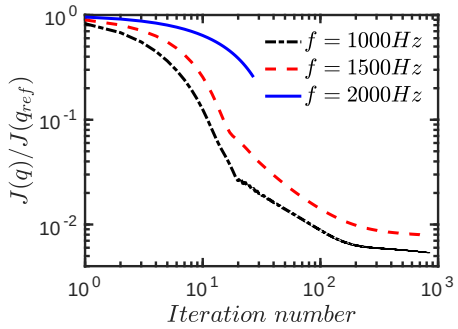

Figure 9: Convergence of $J(q)$ towards a minimum value during the gradient descent optimization at three different input wave packet frequencies – and hence three different $J(q_{ref})$. In all cases, $\lambda = 100$. For $f = 2000$ Hz, the optimization ended soon due to the $|\widetilde{\beta}(s)| \leq 1$ constraint being violated at 0 Hz. This is not the case for the other two frequencies, where computations are terminated manually after vanishing returns upon further iterations.

the inlet towards the outlet as it is modified by the TDIBC. The pressure perturbations measured at the probe location with q_{ref} are shown in Fig. 14(b) in red, where the amplitude of the perturbations has noticeably decreased from the initial 1 Pa value at

parameter	$q_{opt3}(1000Hz)$	$q_{opt3}(1500Hz)$	$q_{opt3}(2000Hz)$
β_∞	5.000000000000000e-01	5.000000000000000e-01	5.000000000000000e-01
τ	4.799390000000000e-04	4.799390000000000e-04	4.799390000000000e-04
$\mathrm{Re}(\tilde{s}_1)$	-4.562252024629700e+03	-5.697035342928950e+03	-3.696840776282980e+03
$\mathrm{Im}(\tilde{s}_1)$	4.462793765578890e+03	7.198059365358520e+03	5.166508778739820e+03
$\mathrm{Re}(\tilde{r}_{1,1})$	-1.607524129467480e+03	-1.377331848071610e+03	-8.004080700521901e+02
$\mathrm{Im}(\tilde{r}_{1,1})$	-7.838523253411610e+02	-1.435002923804180e+03	-1.782905962817980e+03
$\mathrm{Re}(\tilde{r}_{1,2})$	-7.860958562553280e+03	-9.893382513453120e+03	-8.113779825793600e+03
$\mathrm{Im}(\tilde{r}_{1,2})$	-7.016324898782670e+03	-6.255377262186440e+03	-6.915350511607390e+03
$\mathrm{Re}(\tilde{s}_2)$	-2.748396141909810e+04	-2.713188490491970e+04	-2.748569820098920e+04
$\mathrm{Im}(\tilde{s}_2)$	2.008293608242250e+04	2.119014362978530e+04	2.050292728980090e+04
$\mathrm{Re}(\tilde{r}_{2,1})$	-5.031302487269340e+02	4.899832222108420e+02	4.300162080508390e+02
$\mathrm{Im}(\tilde{r}_{2,1})$	-9.811594026017590e+02	-1.638361313973580e+03	-9.032522398700570e+02
$\mathrm{Re}(\tilde{r}_{2,2})$	1.586704986608620e+04	1.351801354536430e+04	1.510898802168430e+04
$\mathrm{Im}(\tilde{r}_{2,2})$	1.953610189966890e+04	2.063895931045980e+04	1.985977048145190e+04

Table 3: q_{opt3} found by optimizing at constant τ and β_∞ for frequency-dependent p'_{tar}.

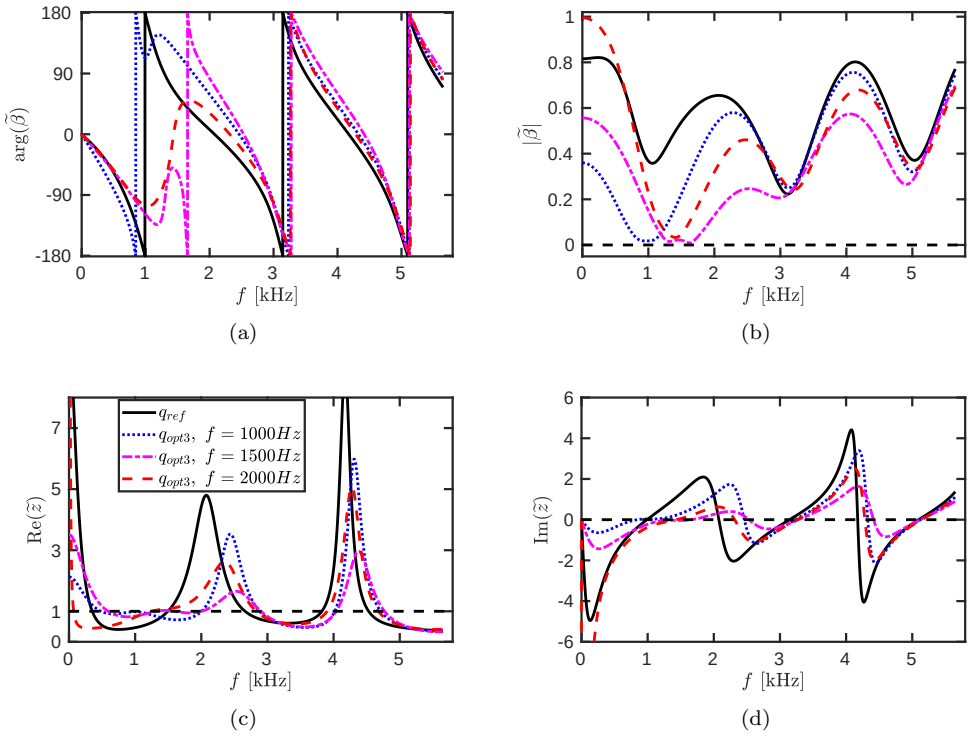

Figure 10: (a) Argument and (b) modulus of the reflection coefficient $\widetilde{\beta}(s)$ based on q_{ref} and q_{opt3} for the three analysed frequencies f. (c) Real and (d) imaginary part of the impedance $\widetilde{z}(s)$. $\widetilde{z} = (1+\widetilde{\beta})/(1-\widetilde{\beta})$.

the inlet. We note, in passing, the effect of the pressure drift discussed at the end of subsection 4.1, which is also visible in Fig. 14(b).

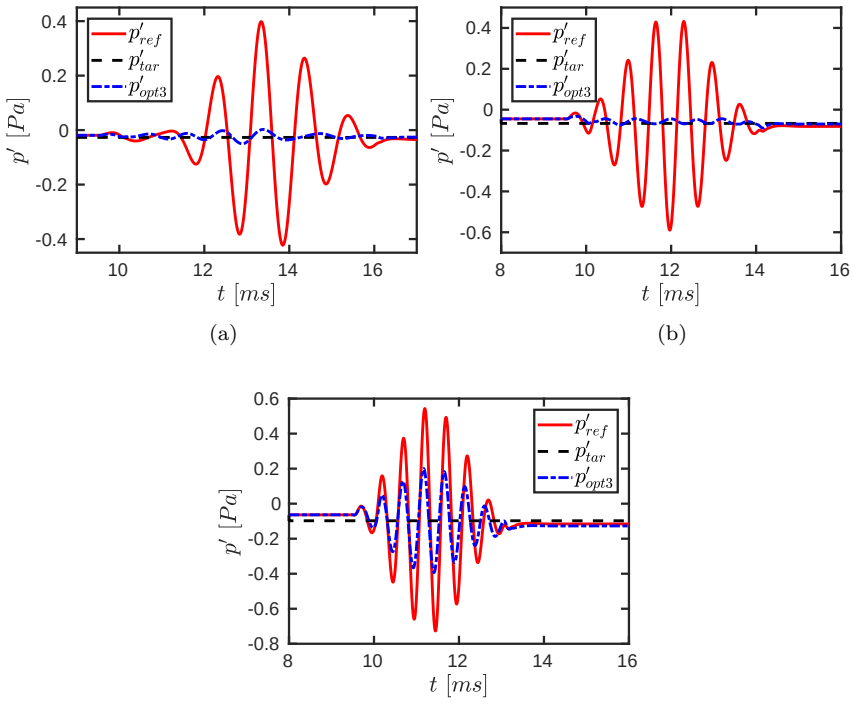

Figure 11: Reflected pressure perturbations (reference and optimized), and target pressure level p'_{tar}. (a) $f = 1000$ Hz, (b) $f = 1500$ Hz, (c), $f = 2000$ Hz.

The attenuation effect of the acoustic liner is most visible in Fig. 15, where the streamwise decrease in the sound pressure levels (SPL) measured along the wall opposite to the TDIBC is plotted. The initial TDIBC parameters in q_{ref} correspond to the ceramic tubular liner (CT57) used in Jones *et al.*[25], and leads to a SPL decrease of 9 dB under the present conditions: an input plane wave packet with frequency centered around $f = 1500$ Hz – see Fig. 2. The choice of this input frequency is justified in Section 5. The optimization procedure followed is identical to that described in the previous section, with constant τ and β_∞. The cost function in Eq. (6) is computed between $t_1 = 1.5$ ms and $t_2 = 10$ ms, and p'_{tar} is taken as constant and equal to the mean of p'_{ref} during that time interval – see Fig. 14(b).

The minimization of the cost function proceeds as shown in Fig. 14(a). After less than 30 iterations, the cost function goes below 10% of its original value. The spatio-temporal evolution of the plane wave packet obtained by using the optimized TDIBC parameters $q_{opt,GIT}$ of Table 4 is displayed in Fig. 13. The perturbations at the probe location and the sound pressure levels across the duct with the optimized TDIBC can be seen in Figs. 14(b) and 15, respectively. Finally, the reactance properties of the optimized liner are displayed in Fig. 16.

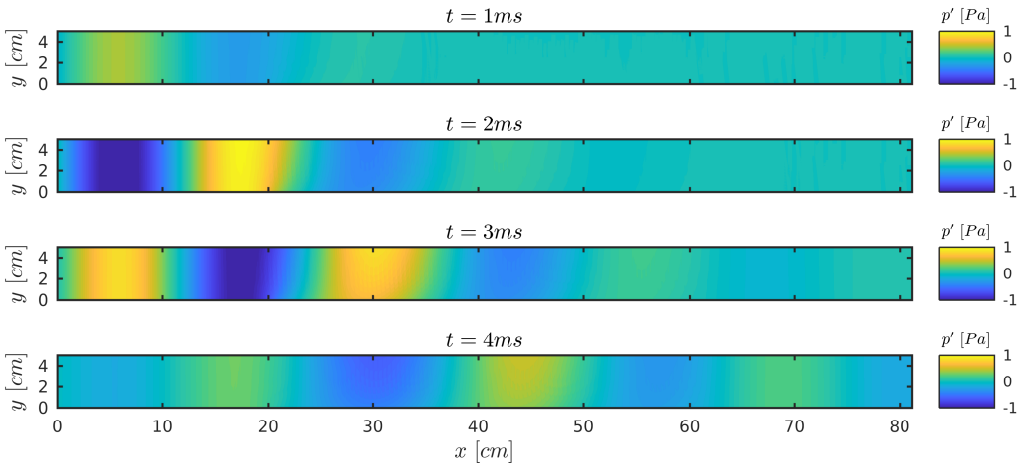

Figure 12: Plane wave packet evolution in the GIT test case, travelling at the speed of sound $c = 344.37$ m/s towards the right. The TDIBC is located at the bottom wall, between 20.3 cm $\leq x \leq$ 60.9 cm – see Fig. 4. Simulation results obtained with the TDIBC parameters before optimization – q_{ref} shown in Table 1.

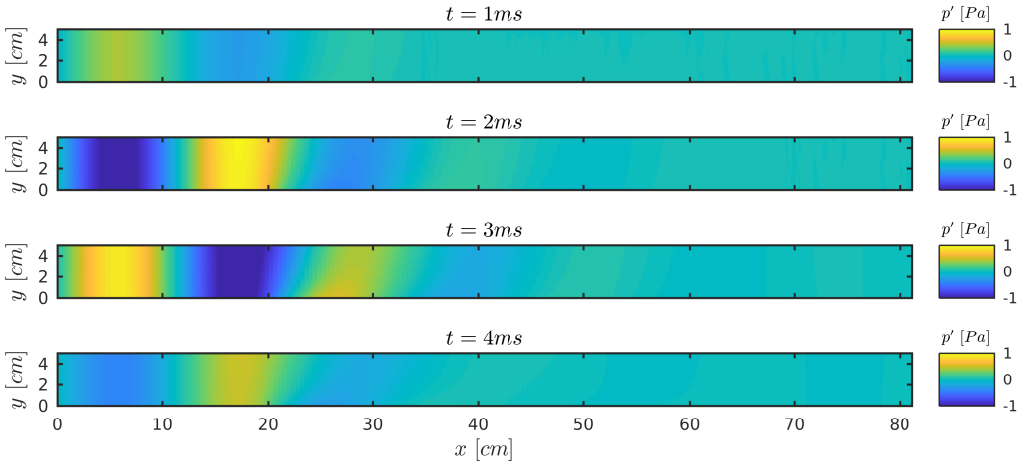

Figure 13: Same as Fig. 12, but simulation results obtained with optimized parameters $q_{opt,GIT}$ with the reactance properties of Fig. 16.

5. Discussion

Before embarking on the discussion, it is convenient to note that a liner with fully absorptive power for perturbations of a single frequency f exhibits an impedance $\tilde{z}$ such that $\mathrm{Re}\,(\tilde{z}) = 1$ and $\mathrm{Im}\,(\tilde{z}) = 0$ at frequency f. That concept proves useful when interpreting the changes induced by the optimization process on the impedance properties

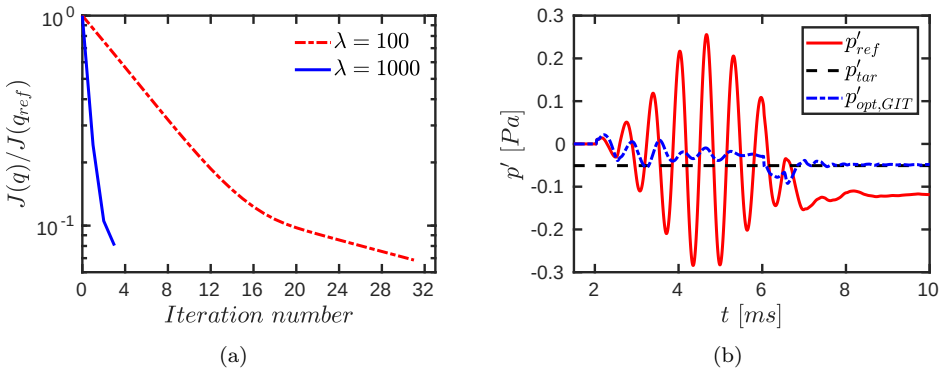

Figure 14: (a) Convergence of $J(q)$ towards a minimum value during the gradient descent optimization. For $\lambda = 100$, $J(q)/J(q_{ref})$ reaches 6.9% while for $\lambda = 1000$, $J(q)/J(q_{ref})$ reaches 8%. In both cases, the optimization is terminated due to the $|\widetilde{\beta}(s)| \leq 1$ condition being violated at $0Hz$. (b) Pressure fluctuations (reference and optimized) at the probe location ($x = 70cm$, $y = 5cm$) for the 2D GIT case, and target pressure level p'_{tar}.

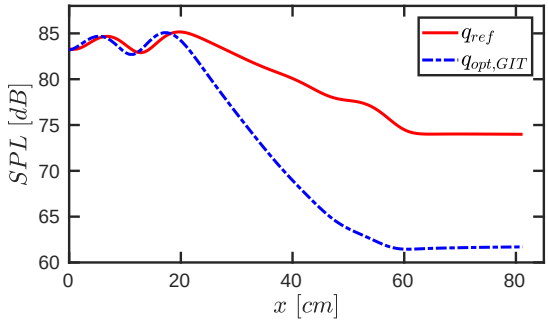

Figure 15: Sound pressure levels measured along the top wall (see Fig. 4) for the input plane wave packet centred around 1500Hz. The TDIBC is located at the bottom wall, between $20.3cm \leq x \leq 60.9cm$.

of the acoustic liner.

The results for the 1D impedance tube are discussed first. It is clear that the optimization process is able to proceed further after setting the bulk reflectivity β_∞ to a constant, yet it is interesting to observe how the acoustic properties of the TDIBC change when going from q_{ref} to q_{opt} in Table 1 by having acted almost exclusively on β_∞. Fig. 6(b) shows that the frequency of the reflection peaks and troughs has not been altered, which is consistent with the poles of q_{opt} remaining almost unchanged from those of q_{ref}. However, the trough around 1 kHz has become shallower with the increase in β_∞. The benefits of increasing β_∞ are less visible on the impedance data in Fig. 6, but a zoom into the curves in Fig. 6(c) close to 1 kHz (not shown) reveals that q_{opt} brings the resistance closer to unity (from below) than q_{ref} does, while the frequency of the zero

parameter	q_{ref}	$q_{opt,GIT}$
β_∞	5.000000000000000e-01	5.000000000000000e-01
τ	4.799390000000000e-04	4.799390000000000e-04
Re(s_1)	-3.816516000000000e+03	-3.734504125380820e+03
Im(s_1)	4.734560000000000e+03	4.912197498313930e+03
Re($\widetilde{r}_{1,1}$)	-7.194232000000000e+02	-9.424292884778670e+01
Im($\widetilde{r}_{1,1}$)	-5.447907000000000e+02	-1.864202983923320e+03
Re($\widetilde{r}_{1,2}$)	-7.179701000000000e+03	-7.491023052287460e+03
Im($\widetilde{r}_{1,2}$)	-7.336684000000000e+03	-7.238922694116080e+03
Re(s_2)	-2.765741000000000e+04	-2.742454898337370e+04
Im(s_2)	2.000290000000000e+04	2.025959879248170e+04
Re($\widetilde{r}_{2,1}$)	1.625807000000000e+03	-1.477206909709660e+02
Im($\widetilde{r}_{2,1}$)	9.996580000000000e+01	-3.484418558326350e+02
Re($\widetilde{r}_{2,2}$)	1.614688000000000e+04	1.577729950072360e+04
Im($\widetilde{r}_{2,2}$)	1.930627000000000e+04	1.959434095246440e+04

Table 4: $q_{opt,GIT}$ is found by optimizing at constant τ and β_∞ in the 2D GIT case. Input plane wave packet centered around $1500Hz$. Found with $\lambda = 100$ after 32 iterations.

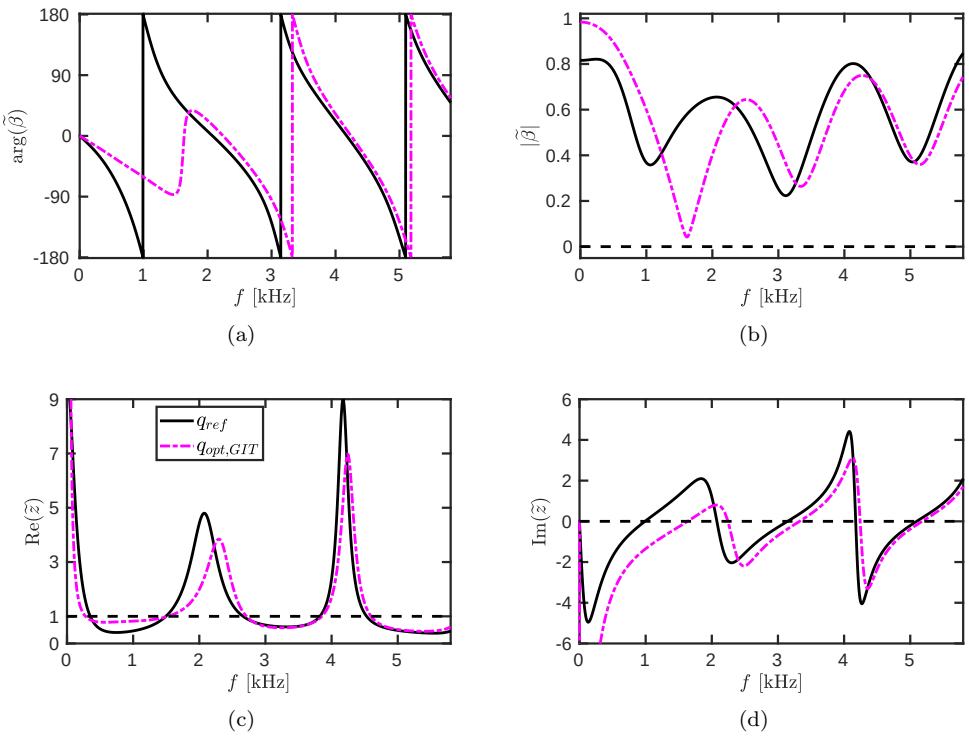

Figure 16: (a) Argument and (b) modulus of the reflection coefficient $\widetilde{\beta}(s)$ based on q_{ref} and $q_{opt,GIT}$. (c) Real and (d) imaginary part of the impedance $\widetilde{z}(s)$. $\widetilde{z} = (1+\widetilde{\beta})/(1-\widetilde{\beta})$.

crossing towards 1 kHz in the reactance curves in Fig. 6(d) remains virtually unchanged.

Setting β_∞ to a constant allows the optimization to act on the oscillatory poles and their corresponding weights, leading to q_{opt2} in Table 1. The resulting parameters drastically improve the absorption properties of the TDIBC. Fig. 6(b) shows that the reflection trough around 1 kHz can be brought down to almost zero, consistent with a resistance closest to unity around that frequency in Fig. 6(c). The range of frequencies over which the reactance remains close to zero has been widened significantly with q_{opt2}, as observed from Fig. 6(d). Comparing p'_{ref} with p'_{opt2} in Fig. 7(b) gives perhaps the most eloquent demonstration of the level of optimization that can be achieved when leaving τ and β_∞ constant for this input frequency centered around 1000 Hz. Keeping the optimization strategy unchanged, different input frequencies are analyzed next.

Fig. 9 shows that similar levels of optimization can be achieved with input wave packets that have amplitude spectra centred around 1000 Hz as well as 1500 Hz, yet for the 2000 Hz case the ability to optimize is severely hindered in comparison. The reason for this – at first surprising – behavior can be found in the constant value of τ. In the lossless limit, a tubular liner can be modelled as a quarter-wavelength resonator with resonant frequencies given by[27]

$$f_n = \frac{(2n+1)c}{4l} \tag{8}$$

where l is the cavity length. Since l and τ are related through $l = c\tau/2$, the first two resonant frequencies obtained with the fixed $\tau = 4.79939 \times 10^{-4}$ s should be around 1042 Hz and 3124 Hz, which is consistent with the first two minima observed in the $|\tilde{\beta}|$ figures based on q_{ref}. The antiresonant frequency for this liner is located halfway in between the two absorption sweet points, *i.e.* close to 2000 Hz. It could therefore be anticipated that without changing the cavity length – and hence τ –, a drop in the optimization capacity should be observed when the frequencies to be attenuated are centred around 2000 Hz compared to 1000 Hz or 1500 Hz. A possible solution to this problem consists in shifting f_n towards higher values by lowering l through τ.

The 2D GIT flow is tackled in better conditions after the lessons learnt from the 1D impedance tube: 1) optimization at constant τ and β_∞ is most effective, and 2) frequencies close to 2000 Hz have limited optimization potential at the chosen τ. The CT57 liner is known to have an effectiveness at cancelling plane monochromatic waves which varies significantly with frequency. For a plane monochromatic wave of frequency 1000 Hz, Jones *et al.*[25] report SPL drops of about 60 dB in the GIT experiment. At 1500 Hz, their data show a much deteriorated SPL drop of about 10 dB. An attempt is made here to find an alternative set of TDIBC parameters that improves upon the performance of the original liner, for frequencies where it is reasonable to expect that its effectiveness can be improved. For all these reasons, an input plane wave packet with amplitude spectrum centered around 1500 Hz is chosen: sufficiently far from the 1000 Hz optimum yet below the 2000 Hz limitations. From Fig. 14(a), it can be concluded that the optimization is able to proceed reasonably far, down to 6.9% of the initial value of the cost function. Although values below 1% are not reached as in the 1D impedance tube – see Fig. 9, it has to be emphasized that here all of the pressure perturbations do not come in contact with the TDIBC, which is only present on one of the two walls. Nevertheless, Fig. 15 illustrates that the original liner decreases the outlet sound pressure level by 9 dB compared to the inlet, and the optimized liner decreases them a further 12 dB. The impedance and reflection properties in Fig. 16 display once again the effect

of the optimization. The reflection minimum in Fig. 16(b) has clearly been lowered and brought closer to the 1500 Hz range of frequencies.

The location of the probe at which the perturbations are minimized will necessarily have an effect on the resulting set of optimized TDIBC parameters. But the freedom to choose the probe location also allows one to be able to target more selectively where the perturbations ought to be minimized. Another possibility would be, of course, to embed into the cost function a pressure – or sound intensity – that is integrated throughout the outlet. It is only a matter of choice which does not imply any difficulty from an implementation point of view, since automatic differentiation can cope with any cost function definition as long as its expression can be differentiated.

The results shown so far are sufficient to illustrate that the optimization process can lead to different sets of optimized TDIBC parameters, even when starting from identical initial parameters q_{ref} and keeping the input signal spectra unchanged. This can be seen by comparing, for instance, q_{opt3} at 1500 Hz in Table 3 with $q_{opt,GIT}$ in Table 4 – which is also obtained with the same input amplitude spectrum. Different flow conditions lead to different TDIBC optima, that is not surprising. What one may want to further assess, however, is how different two optima will be when all that is changed is the initial set of TDIBC parameters. That is assessed in Fig. 17. The different data have been obtained by changing each element of q_{ref} – except for β_∞ and τ – through multiplication by $(1+\theta)$, where θ is chosen from a uniform random distribution spanning the range $-|q_{ref}(m)|R \leq \theta \leq |q_{ref}(m)|R$. For $R = 0.1$ and $R = 0.2$, the convergence towards a minimum is plotted in Fig. 17. It appears that changing the initial set of values of q_{ref} by up to 10% of their original value marginally modifies the optimum state, while the same test but with changes of up to 20% leads to an entirely different optimum. The conclusion drawn is that the initial q_{ref} has a significant impact on the minimum that is found at the end of the optimization procedure, so that a poor choice of the initial q_{ref} cannot, in general, be compensated by the optimization approach brought forward here. In the present study, the initial set of conditions is guided by the CT57 liner, which is already a fairly effective design that places the optimization procedure not too far away from optimum. In the work by Özkaya *et al.*[11], a first-stage, low-fidelity optimization is applied before the gradient descent algorithm, which is similar to placing the multi-parameter space reasonably close to optimal values before diving in the search for an optimum point.

6. Conclusions

Numerical simulations are carried out using JAGUAR, a flow solver that features the possibility to apply a TDIBC[13]. The parameters that control the behavior of the TDIBC are based on the oscillo-diffusive representation (ODR) of the acoustic reflection operator[12, 22], with values chosen to reproduce accurately the properties of the ceramic tubular liner CT57[25]. The TDIBC parameters are modified in order to optimize the behavior of the TDIBC at dampening pressure perturbations with different broadband frequency contents. The optimization follows a gradient descent algorithm, where the gradients of the cost function with respect to the ODR parameters has been obtained by means of the automatic differentiation compatibility of JAGUAR[24].

A 1D impedance tube test case is considered first, which reveals that optimizing the TDIBC at constant bulk reflectivity β_∞ and time delay τ proves most effective - as

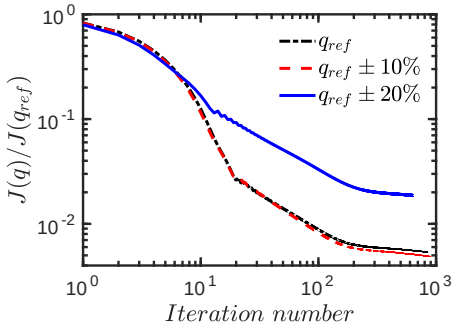

Figure 17: Convergence of $J(q)$ towards a minimum value during the gradient descent optimization, with $f = 1000Hz$ and $\lambda = 100$ in all cases. Two convergence curves are obtained by perturbing each element of q_{ref} by a random factor of up to ± 0.1 (or ± 0.2) of its value.

opposed to letting these two parameters vary. Radically improved dampening properties compared to the original TDIBC are obtained following this strategy. The effectiveness of the optimization is found to be limited when the input perturbations come close to the anti-resonant frequency of the tubular liner modelled by the TDIBC. An obvious workaround to this limitation is to carry out the optimization by keeping τ constant yet fixed to a smaller value. Finally, a 2D test case of the GIT is chosen to study a more realistic flow configuration, where the liner is known to be operating at off-design conditions. The optimization succeeds at adapting the set of TDIBC parameters to recover an improved absorptive performance.

Throughout the present work, the optimization is applied to quantities appearing in the ODR of the acoustic liner's reflection operator. For liners characterized by few and simple geometric quantities, there are mathematical models that can approximate the corresponding ODR coefficients describing the reflection or impedance properties. The converse is not as trivial, since not all impedance properties can be realized using a geometry-based mathematical model. As a consequence, it is not guaranteed that the optimized parameters found in the present work can be generated with a modified CT liner. Since the bulk reflectivity and the tube length are fixed, the remaining free parameter that can change the CT liner impedance is the tube diameter alone. That will not suffice to select the values of the 12 parameters left to adjust within the parameter vector q. Additional geometric parameters would be needed in the mathematical model, which would for instance involve tubes of more complex cross-section. As a result, improvements to the present approach include using the geometry-based mathematical model inside the flow solver, with routines that translate the geometrical parameters directly into ODR coefficients. In this manner, the optimization could be carried out based on updates of the input geometric parameters rather than on the ODR coefficients, thus limiting the optimization space to the realm of readily obtainable acoustic liners.

7. Acknowledgments

This work was part of the 3C2T project, which was financially supported by the STAE foundation (Science and Technology for Aeronautics and Space) through grant number CDT-R050-L00-T00. The project involved the French aerospace laboratory (ONERA) through the internal project JEROBOAM, the European Center for Research and Advanced Training in Scientific Computation (CERFACS) and the Institute of Fluid Mechanics of Toulouse (IMFT) under the supervision of Christophe Airiau (IMFT). J.I.C. acknowledges funding from the People Program (Marie Curie Actions) of the European Union's Seventh Framework Program (FP7/2007-2013) under REA grant agreement n. PCOFUND-GA-2013-609102, through the PRESTIGE program coordinated by Campus France. J.I.C. is grateful to R. Roncen for enlightening discussions on interpreting impedance and reflection data.

References

References

[1] K. J. Baumeister, Evaluation of optimized multisectioned acoustic liners, AIAA Journal 17 (11) (1979) 1185–1192. doi:10.2514/3.61299.

[2] T. Law, A. Dowling, R. Corral, Optimisation of axially segmented liners for aeroengine broadband noise, Journal of Sound and Vibration 329 (21) (2010) 4367–4379.

[3] C. Gerhold, M. Jones, M. Brown, Segmented liner to control mode scattering, in: 19th AIAA/CEAS Aeroacoustics Conference, 2013, p. 2078. doi:10.2514/6.2013-2078.

[4] L. Campos, J. Oliveira, On the optimization of non-uniform acoustic liners on annular nozzles, Journal of Sound and Vibration 275 (3) (2004) 557–576. doi:https://doi.org/10.1016/j.jsv.2003.06.035.

[5] D. Nark, M. Jones, Broadband liner optimization for the source diagnostic test fan, in: 18th AIAA/CEAS Aeroacoustics Conference (33rd AIAA Aeroacoustics Conference), 2012, p. 2195.

[6] D. Nark, M. Jones, D. Sutliff, Modeling of broadband liners applied to the advanced noise control fan, in: 21st AIAA/CEAS Aeroacoustics Conference, 2015, p. 2693.

[7] D. Nark, M. Jones, Further development and assessment of a broadband liner optimization process, in: 22nd AIAA/CEAS Aeroacoustics Conference, 2016, p. 2784.

[8] D. L. Sutliff, D. M. Nark, M. G. Jones, N. H. Schiller, Design and acoustic efficacy of a broadband liner for the inlet of the DGEN aero-propulsion research turbofan, in: 25th AIAA/CEAS Aeroacoustics Conference, 2019, p. 2582.

[9] E. Özkaya, J. Abdel Hay, N. R. Gauger, F. Thiele, Development of an adjoint caa solver for design optimization of acoustic liners, in: 22nd AIAA/CEAS Aeroacoustics Conference, 2016, p. 2778.

[10] E. Özkaya, J. A. Hay, N. R. Gauger, N. Schönwald, F. Thiele, A two-level approach for design optimization of acoustic liners, in: Proceedings of 9th international conference on computational fluid dynamics, ICCFD9-2016-184, 2016.

[11] E. Özkaya, N. R. Gauger, J. A. Hay, F. Thiele, Efficient design optimization of acoustic liners for engine noise reduction, AIAA Journal 58 (3) (2020) 1140–1156.

[12] F. Monteghetti, D. Matignon, E. Piot, L. Pascal, Design of broadband time-domain impedance boundary conditions using the oscillatory-diffusive representation of acoustical models, The Journal of the Acoustical Society of America 140 (3) (2016) 1663–1674.

[13] R. Fiévet, H. Deniau, E. Piot, Strong compact formalism for characteristic boundary conditions with discontinuous spectral methods, Journal of Computational Physics 408 (2020) 109276.

[14] A. Cassagne, J. Boussuge, N. Villedieu, G. Puigt, I. D'ast, A. Genot, Jaguar: a new CFD code dedicated to massively parallel high-order LES computations on complex geometry, in: The 50th 3AF International Conference on Applied Aerodynamics (AERO 2015), 2015.

[15] American Society of Mechanical Engineers Digital Collection, Comparison of various CFD codes for LES simulations of turbomachinery: from inviscid vortex convection to multi-stage compressor, Vol. 2C: Turbomachinery.

[16] Y. Liu, M. Vinokur, Z. J. Wang, Spectral difference method for unstructured grids I: basic formulation, Journal of Computational Physics 216 (2) (2006) 780–801.
[17] D. Kopriva, A staggered-grid multidomain spectral method for the compressible navier–stokes equations, Journal of Computational Physics 143 (1) (1998) 125–158.
[18] A. Jameson, A proof of the stability of the spectral difference method for all orders of accuracy, Journal of Scientific Computing 45 (1-3) (2010) 348–358.
[19] K. Van den Abeele, C. Lacor, Z. Wang, On the stability and accuracy of the spectral difference method, Journal of Scientific Computing 37 (2) (2008) 162–188.
[20] J. Vanharen, G. Puigt, X. Vasseur, J. Boussuge, P. Sagaut, Revisiting the spectral analysis for high-order spectral discontinuous methods, Journal of Computational Physics 337 (2017) 379–402.
[21] J. Berland, C. Bogey, C. Bailly, Low-dissipation and low-dispersion fourth-order Runge–Kutta algorithm, Computers & Fluids 35 (10) (2006) 1459–1463.
[22] F. Monteghetti, D. Matignon, E. Piot, Energy analysis and discretization of nonlinear impedance boundary conditions for the time-domain linearized euler equations, Journal of Computational Physics 375 (2018) 393–426.
[23] L. Hascoët, V. Pascual, The Tapenade automatic differentiation tool: principles, model, and specification, ACM Transactions on Mathematical Software (TOMS) 39 (3) (2013) 20.
[24] J. Cardesa, L. Hascoët, C. Airiau, Adjoint computations by algorithmic differentiation of a parallel solver for time-dependent pdes, Journal of Computational Science 45 (2020) 101155. doi:https://doi.org/10.1016/j.jocs.2020.101155.
[25] M. Jones, W. Watson, T. Parrott, Benchmark data for evaluation of aeroacoustic propagation codes with grazing flow, in: 11th AIAA/CEAS Aeroacoustics Conference, 2005, p. 2853.
[26] T. J. Poinsot, S. K. Lele, Boundary conditions for direct simulations of compressible viscous flows, Journal of Computational Physics 101 (1992) 104–129.
[27] F. Monteghetti, Analysis and discretization of time-domain impedance boundary conditions in aeroacoustics, Thesis, Institut Supérieur de l'Aéronautique et de l'Espace (ISAE-SUPAERO) ; Université de Toulouse (October 2018).